

pubs.acs.org/JPCC Article

Cupric Oxide Mie Resonators

Sundaram Bhardwaj Ramakrishnan, Nishan Khatri, Ravi Teja Addanki Tirumala, Farshid Mohammadparast, Krishnageetha Karuppasamy, A. Kaan Kalkan, and Marimuthu Andiappan*



Cite This: J. Phys. Chem. C 2022, 126, 16272-16279



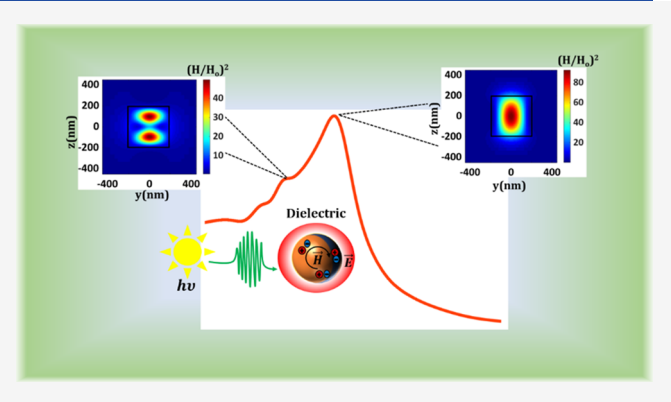
ACCESS I

Metrics & More

Article Recommendations

Supporting Information

ABSTRACT: In the past two decades, plasmonic Mie resonators enabled numerous breakthroughs in the manipulation of light at the subwavelength scale as well as at larger scales through the construction of metamaterials/surfaces from them, as artificial atoms. Central to these features are enhanced field concentrations and extinction cross sections at Mie resonances. These unique aspects are also exhibited by moderate-to-high refractive index dielectric Mie resonators. Dielectric Mie resonators offer further unique attributes, such as magnetic resonances and low losses. Here, we report on submicron cupric oxide (CuO) particles with a medium refractive index that can exhibit strong electric and magnetic Mie resonances with extinction/scattering cross sections as large as those of plasmonic resonators. Through the develop-



ment of particle synthesis techniques enabling shape and size control, optical spectroscopy, and finite-difference-time-domain simulations, we show the Mie resonance wavelengths are size- and shape-dependent. This spectral tunability in the visible-to-near-infrared regions allows for energy harvesting and light manipulation in a wider range of the solar spectrum. The strong electric and magnetic Mie-resonance-mediated nanoantenna attribute of CuO particles can be potentially exploited in applications, such as metamaterials/surfaces, photocatalysis, and photovoltaics.

■ INTRODUCTION

The optical antenna (i.e., nanoantenna) effect has been instrumental in nano-optics. Similar to that of radio wave and microwave antennas, its attribute is to localize electromagnetic (EM) fields by transforming free propagating radiation and vice versa. 1,2 Optical antennas can enhance and facilitate several photophysical processes. In a light-emitting diode (LED), recombination of an electron-hole pair generates a photon. In photovoltaics, the reverse process occurs, where an incoming photon generates an electron-hole pair. In both cases, an optical antenna mediates the coupling of charge oscillations (plasmonic or dielectric Mie modes) with the photon and localizes it to make the process more efficient.³ Optical antennas also enhance photophysics in molecules, such as absorption, fluorescence, and Raman scattering. Hence, they enable trace-level/single molecule spectroscopy, 4-7 ultrasensitive light detection, 8,9 biosensing, 10 and heat transfer. 11,12 In recent years, the development of optical antennas has mainly relied on plasmonic metal nanostructures (PMNs). Numerous applications of PMNs have been demonstrated, such as sensors, 13 nano-, and micro-optical devices, 14 photocatalysis, 15-21 and photovoltaics. 22-28 PMNs exhibit high extinction cross sections due to localized surface plasmon resonance (LSPR). $^{16,29-32}$ The LSPR frequency is sensitive to dielectric function and geometry (shape and size) of the nanostructure as well as the physical environment and EM

coupling between neighboring nanostructures and substrates.^{33,34} However, plasmonic resonators suffer from absorption losses inherent to metals at visible frequencies.³⁵

Further, scaling up the fabrication of metal nanostructures via top-down approaches, as in current semiconductor microfabrication, has not yet been realized.^{35,36} To overcome these challenges, there has been a growing interest in developing novel dielectric, Mie-resonator nanoparticles. These alternative materials can allow for light manipulation at the nanoscale and still exhibit strong extinction cross sections. 32,35,37 The dielectric nanostructures exhibit both the electric and magnetic multipolar modes, namely, dielectric Mie modes, that can mediate the optical antenna effect. Unlike in plasmonic resonators, the electric resonances in dielectric Mie resonators are driven by the oscillation of polarization charges bound to covalent bonds (in contrast to delocalized electrons in metallic bonds), while the magnetic resonances are driven by displacement currents (rather than actual currents). 35,37 Numerous nano-optics applications may be conceived, such as

Received: July 1, 2022
Revised: September 2, 2022
Published: September 15, 2022





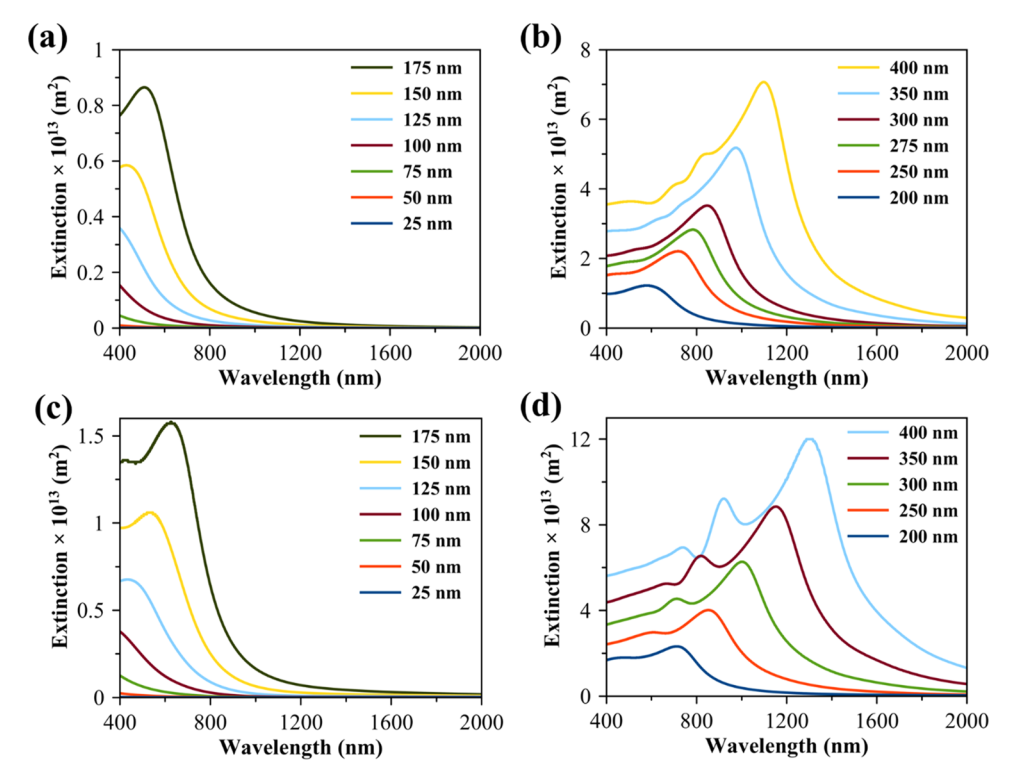


Figure 1. Simulated extinction cross-section spectra of CuO spheres (a, b) and cubes (c, d) for various sizes (diameters and edge lengths are given in the legend, respectively). For the cubes, the incident radiation propagates along one of the principal axes.

optical sensors, nonlinear optics, surface-enhanced absorption, fluorescence and Raman scattering, directional scattering, photocatalysis, and photovoltaics. 2,32,37-41

Recent computational and experimental investigations by Andiappan and co-workers have established that Mie resonances in dielectric cuprous oxide (Cu₂O) cubes and spheres can be tailored through size. ^{32,37,42} These reports show that Cu₂O cubes and spheres exhibit strong enhancement of electric as well as magnetic fields at Mie resonances, accounting for high scattering cross sections (e.g., 7 times that of the geometric cross section for a 300 nm size cube, that is, scattering efficiency = 7). These strong Mie resonances in Cu₂O subwavelength structures are owed to moderate refractive index (real part), n_i in the range of 2.6–3.1 over the wavelength range of 400-2000 nm. 43 Additionally, the lowest band gap of 2.15 eV is dipole-forbidden, and hence an imaginary part of the refractive index (k) and losses are sufficiently low up to the second gap (direct and dipoleallowed) of 2.6 eV (480 nm). Therefore, strong Mie resonances can be sustained in the range of 480-2000 nm. The general criterion for moderate *n* is $1.7 \lesssim n \lesssim 3.0$, which allows spectral overlapping of magnetic and electric resonances, enabling directional scattering (Kerker effect).⁴⁴ This interesting attribute is lost if n > 3, upon which the magnetic and electric resonances are spectrally separated from each other.44

Cupric oxide (CuO) has similar material properties to $\mathrm{Cu_2O}$ in the wavelength range of 500–2000 nm (i.e., $2.5 \lesssim n \lesssim 3.0$ and sufficiently low k), 43,45,46 promising of dielectric Mieresonators. In this contribution, we report dielectric Mieresonances in subwavelength nanostructures of CuO. Specifically, we focus on the synthesis and characterizations of submicron CuO particles and the elucidation of the Mie

resonances in them by finite-difference time-domain (FDTD) simulations and single-particle scattering measurements.

EXPERIMENTAL DETAILS

To prepare submicron CuO particles, we first prepared submicron Cu_2O particles using solution-based synthesis protocols reported in our recent contribution. Using these solution-based synthesis protocols, Cu_2O quasi-spherical and cubical particles of controlled sizes in the range of ~40–450 nm were prepared. CuO particles were then prepared through the oxidation of solution-synthesized submicron Cu_2O particles in a tubular furnace at 500 °C. The detailed procedure for the preparation and characterization of CuO particles and the details of FDTD simulations are provided in the Supporting Information (SI).

■ RESULTS AND DISCUSSION

To predict the dielectric Mie resonances in CuO particles of different sizes and shapes, we performed FDTD simulations for CuO nanospheres and nanocubes of different sizes. The simulated extinction spectra for the CuO spheres and cubes are shown in Figure 1a-d for different particle sizes from 25 to 400 nm. With increasing particle size, for both spheres and cubes, the extinction cross section increases, and the resonance peaks redshift, as reported by others. 35,37,44 When the diameter/edge reaches and exceeds 200 nm, there are multiple Mie resonance peaks spread across the simulation window of 400-2000 nm. For example, the largest simulated sphere shown in Figure 1b is 400 nm in diameter, where the two dipolar resonances (electric and magnetic, spectrally overlapped) occur at photon energies below the band gap of CuO (i.e., wavelengths longer than 1033 nm). CuO is a p-type semiconductor with an indirect band gap of ~1.2 eV. 49 These resonance features are not seen in the absorption or reflectance

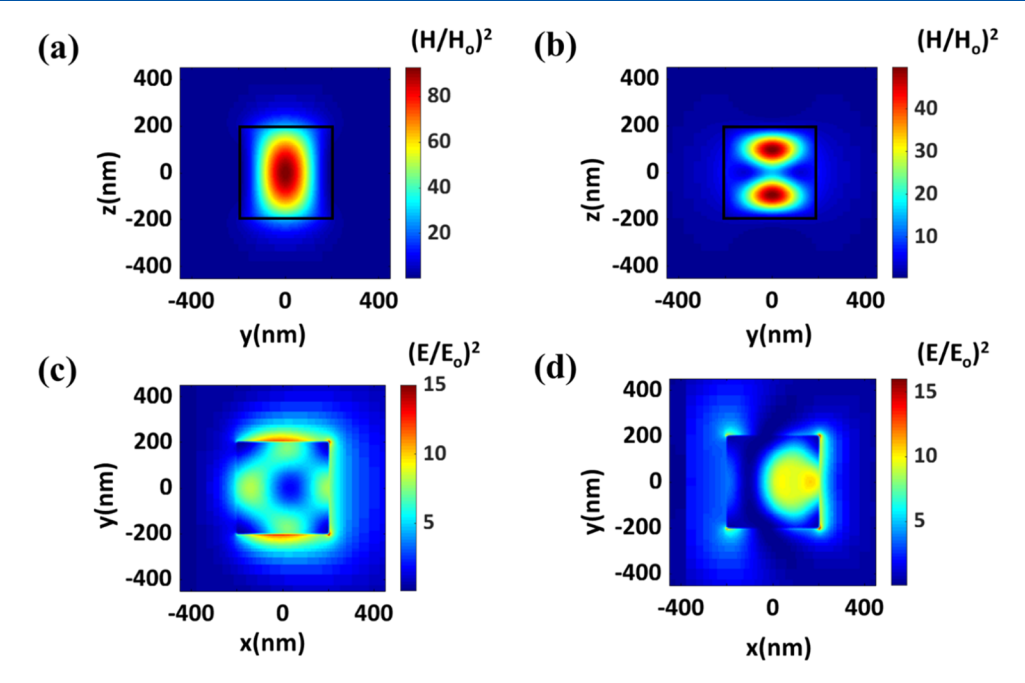


Figure 2. Simulated spatial distribution of enhancement in (a, b) magnetic field intensity $[H^2/H_0^2]$ in the YZ plane and (c, d) electric field intensity $[E^2/E_0^2]$ in the XY plane for a CuO cube of 400 nm edge length. The enhancement is over the far-field incident field (subscript 0). Panels (a) and (c) represent the lowest energy resonance (1296 nm). Panels (b) and (d) represent the second-lowest energy resonance (935 nm).

spectra of bulk single crystalline CuO. In the SI, we also show that scattering becomes the dominant contribution to Mie extinction (i.e., over absorption) beyond particle size of 250 nm for spheres as well as cubes (Figures S2–S5 in the SI). Therefore, larger CuO nanoparticles can be employed as efficient scatterers.

To have a better understanding of the Mie resonances observed in the extinction spectra of CuO particles (Figure 1a-d), we performed a detailed analysis of the simulated data for 400 nm cubic particles. Specifically, in analyzing the multiple Mie resonances observed in the extinction spectrum of the 400 nm cubic particles (Figure 1d), we mapped the magnetic and electric field distributions at multiple wavelengths around the lowest and second-lowest energy resonance frequencies in Figure 2, at 1296 and 935 nm, respectively. The magnetic field distributions at these two wavelengths are plotted in Figure 2a,b, respectively. The electric field distributions are mapped in Figure 2c,d, respectively. For generating the field distributions in the simulation, a plane wave is used for propagation in the direction of the positive *x*axis and polarized along the y- and the z-axes for the electric and magnetic fields, respectively. The detailed simulation procedure is described in the SI.

The magnetic field patterns at the lowest resonance peak wavelength shown in Figure 2a confirm the presence of magnetic dipole mode. Similarly, the electric field patterns at the lowest resonance peak wavelength shown in Figure 2c exhibit a two-lobe distribution, which is a characteristic trait of an electric dipole. The enhanced magnetic field patterns (e.g., Figure 2a) are generated by the circular displacement currents resulting from a strongly coupled electric field penetrating the particle. The resulting magnetic response is made possible when the particle size (diameter, d) and wavelength in the particle medium (λ/n) are comparable ($d \sim \lambda/n$), where λ is the wavelength in free space. This simple scaling relation also explains the tunability of the resonance with geometry. From the FDTD simulation results in Figure 2a-d along with the

results shown in Figure S6a—d in the SI, it can be concluded that the lowest energy Mie resonance peak is associated with the combination of the magnetic and electric dipole excitations. Similarly, it is concluded that both the magnetic and electric quadrupole excitations contribute to the second-lowest energy Mie resonance, being at 935 nm. The results also show that the 400 nm CuO cubic particle can exhibit field localization and enhancement of up to 80 and 15 for the magnetic and electric local field intensities, respectively, over the incident far field.

To experimentally confirm the tunable Mie resonances in CuO particles, we characterized the CuO particles by singleparticle scattering spectroscopy. The CuO particles are prepared through the oxidation of Cu₂O particles, and the formation of CuO particles is confirmed using X-ray diffraction (XRD) patterns and Raman spectra of samples measured before and after oxidation. Figure 3a,b depicts XRD spectra for Cu₂O and CuO, that is, before and after oxidation. The assignment of facets of Cu₂O in Figure 3a was referred from previous reports by Andiappan and co-workers. 32,37,42 Similarly, the peak assignment of CuO facets in Figure 3b was sourced from the literature. 46,51-54 From the comparison of the transmission electron microscopy (TEM) images of Cu₂O particles (i.e., before oxidation) and CuO particles (i.e., after oxidation), we find that the morphology of particles changes upon oxidation. For example, Figure 3c shows the representative TEM image of Cu_2O cubes of 426 \pm 63 nm edge length. Upon oxidation into CuO, the addition of oxygen increases the particle size to 530 ± 49 nm (Figure 3d). This change in size is expected mainly because CuO (monoclinic) is a denser phase with a density of 6.3 g/cm³, versus 6.0 g/cm³ of Cu₂O (cubic). Also, for the Cu₂O cubes sample shown in Figure 3c, the shape changes upon oxidation from regular cubes to irregular CuO rectangular prisms with rounded corners/edges and quasi-spheres (e.g., Figure 3d).

Figure 3e shows the Raman spectrum of solutionsynthesized submicron Cu₂O particles before oxidation. The

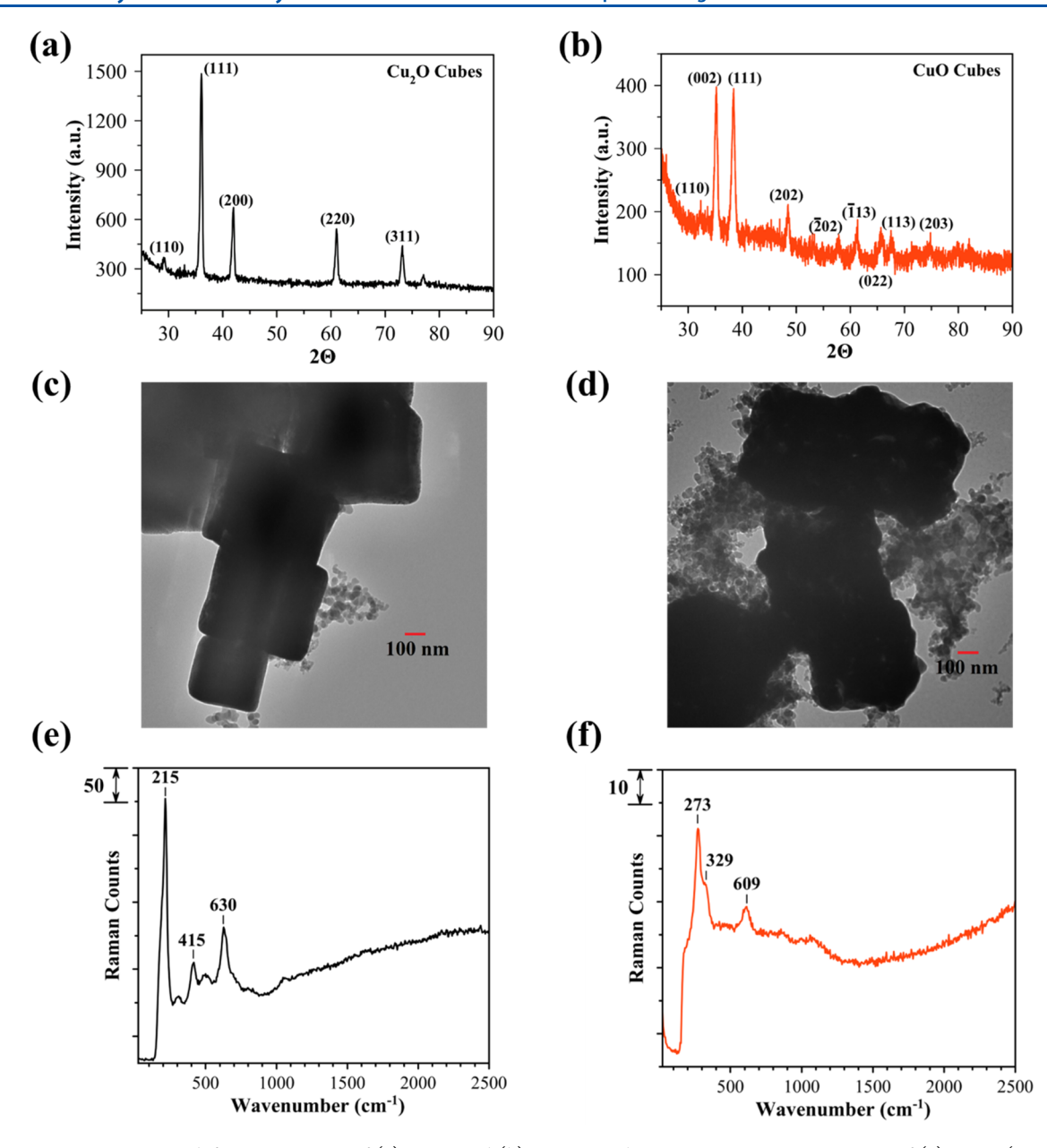
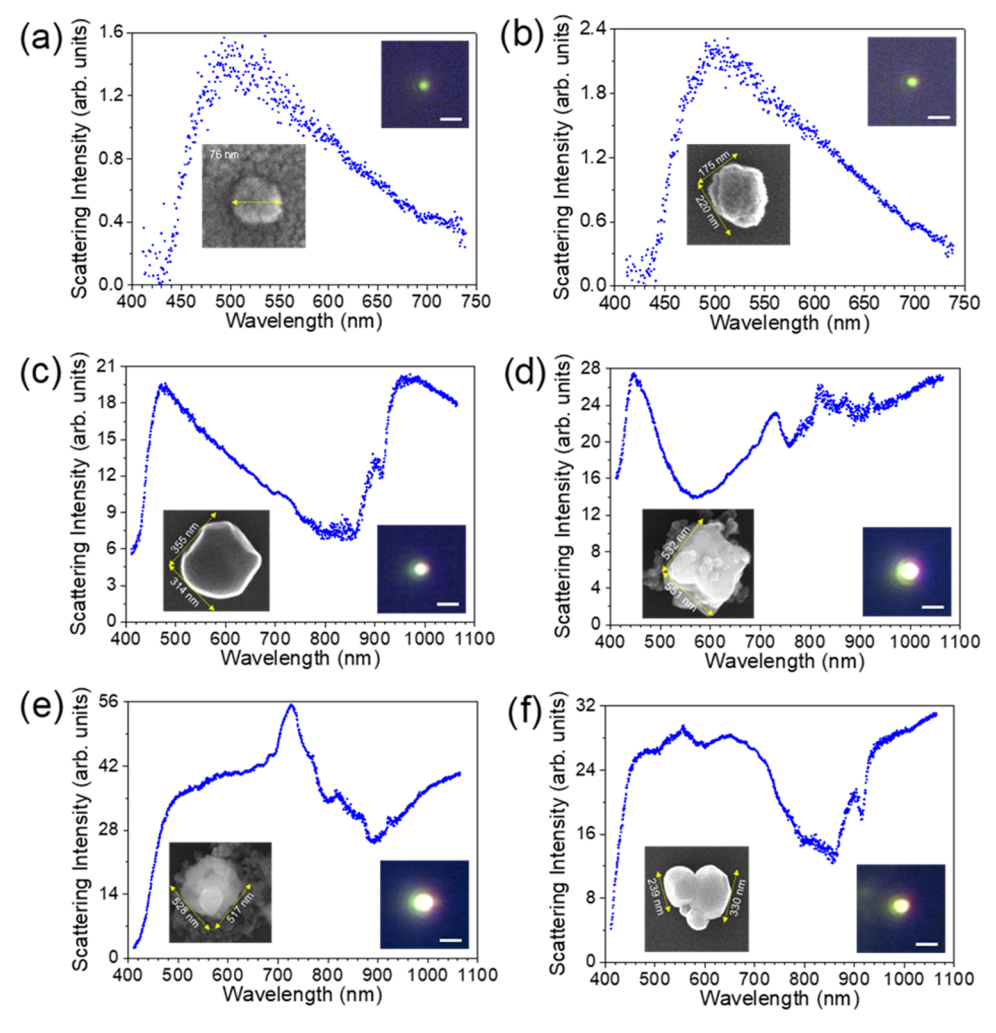


Figure 3. Representative X-ray diffraction patterns of (a) Cu_2O and (b) CuO particles. Representative TEM images of (c) Cu_2O (426 \pm 63 nm) and (d) CuO particles (530 \pm 49 nm). Representative Raman spectra of (e) Cu_2O and (f) CuO particles.

strong peak at 215 cm $^{-1}$ is assigned to a second-order overtone, $2\Gamma_{12}^{-}$, which is a characteristic in modes in crystalline $Cu_2O.^{37}$ Similarly, another strong peak at 630 cm $^{-1}$ is assigned to the infrared-allowed Γ_{15}^{-} (TO) mode in Cu_2O crystals. Finally, the weak peak at 415 cm $^{-1}$ is attributed to the overtone of four phonons, $3\Gamma_{12}^{-}+\Gamma_{25}^{-}$ in crystalline $Cu_2O.^{37}$ Additionally, Figure 3f displays the Raman spectrum of the submicron particles after oxidation in a tubular furnace at 500 °C. The strongest peak at 273 cm $^{-1}$ is assigned to the A_{1g} mode, which characterizes the monoclinic crystal structure of $CuO.^{55-57}$ Similarly, the Raman peaks at 330 and 609 cm $^{-1}$ correspond to B_{1g} and B_{2g} modes of the monoclinic structure in crystalline $CuO.^{55-57}$ Hence, the Raman spectra shown in Figure 3e,f confirm the complete oxidation of the as-synthesized Cu_2O particles to CuO particles.

We have validated the strong and tunable Mie resonances in CuO particles by single-particle scattering spectroscopy, as

shown in Figure 4. The details of the experimental setup, sample preparation, acquisition, and data analysis for scattering measurements are described in the SI. Figure 4a shows the Mie scattering spectrum of a 76 nm size particle, for which a sharp drop occurs below 490 nm. We attribute this cutoff to an optical gap in CuO at ~2.5 eV, 45,46 over which direct and dipole-allowed electron transitions (absorption) dominantly dephase the excited Mie mode and thereby absorption outcompetes scattering. The same is observed in the other five spectra, as well. The simulations do not capture this fall in scattering (Figure S2 in SI) because the solved Maxwell equations employ the dielectric function of the bulk CuO. A detailed explanation of this observation is the subject of a future report. Hence, Figure 4a does not present a Mie resonance peak in the spectral range of the scan. On the other hand, the spectrum of the 220 nm size (long axis) particle in Figure 4b hints at a resonance peak developing at about 500



pubs.acs.org/JPCC

Figure 4. Representative single-particle scattering spectra of (a, b) spherical (smaller), (c-e) faceted (larger), and (f) aggregated CuO particles. Scattering Intensity is as defined/computed in the SI. Scanning electron microscopy (SEM) and optical images of the particles are also displayed. The scale bars in the optical images are 2 μ m.

nm, right before the cutoff at the optical gap. Here, the particle shape is close to an ellipsoid with a long-to-short axis ratio of 1.26, and simulations for a 200 nm size sphere also reveal a Mie resonance close to 500 nm.

Next, we look at the scattering spectra of larger particles in Figure 4c-e, which were acquired in the spectral range of 400–1000 nm. The granular particle in Figure 4c with rounded corners/edges, whose plan view appears to be halfway between a rectangle and circle, with long and short axes of 355 and 314 nm, respectively, exhibits a strong resonance band at 975 nm. Compared with the simulated scattering spectra for spheres and cubes, we anticipate this band is associated with the electric and magnetic dipolar resonances with incident propagation direction along the long axis (355 nm). The lowest energy resonance for simulated spheres of 350 nm diameter is found exactly at the same wavelength. Further, we calculate a scattering cross section of 3.2×10^{-13} m² for the peak of this resonance band, which is close to the simulation value of 3.8×10^{-13} m² for a 350 nm diameter sphere (see Figure S2b). Close to the 975 nm band, we also observe a resonance band at 900 nm, which we associate with the electric and magnetic dipolar resonances with excitation along the short axis (314 nm). Hence, the broken symmetry by asymmetric particle shape leads to the observation of a higher

number of resonance peaks. In the experiment, the single particles were excited using a darkfield condenser at glancing incidence (18°) to the substrate uniformly from all directions. The light scattered to the far field in the semi-infinite space around the particle (above the substrate) was collected by a high-numerical-aperture lens. Hence, it is possible to excite all of the dielectric modes of the particle propagating parallel to the substrate.

For the even larger particles in Figure 4d,e, the electric and magnetic dipolar resonances are inferred to have shifted to longer wavelengths, being out of the scan range, as the tail of a strong resonance band is seen at the upper end of the measurement range (1064 nm), being consistent with the simulations (i.e., as in 400 nm size sphere and cube). For these two largest particles, we observe debris of smaller particles possibly produced during the oxidation of Cu₂O cubes at 500 °C, as they are not present among the as-synthesized Cu₂O cubes. Due to the smaller particle size of less than ~100 nm, Mie resonances of these smaller particles occur in UV, and the scattering intensity is expected to be insignificant, as inferred from the simulation results of Figure S2. Theoretically, the scattering cross section of dipolar resonances scale with the sixth power of the particle size.⁵⁸ Therefore, the smaller particles should not contribute to the scattering spectra in

Figure 4d,e. Additionally, these spectra exhibit artifact peaks at 810, 864, and 917 nm due to the hot mirror filter employed. Despite normalization of the raw spectrum by standard spectrum after background subtraction (SI), these three peaks could not be eliminated in these spectra, possibly due to the low counts in the 800–930 nm interval. Another effect of annealing at 500 °C has been the sintering of the nanoparticles. Accordingly, we included the scattering spectrum of a clump of sintered particles of varying sizes (Figure 4f). In this spectrum, multiplicity of resonance bands spread over the 500–1100 nm range is seen due to varying sizes of the nanoparticles (140–330 nm).

In summary, the experiment shows differences from simulations due to irregularities and asymmetry in particle shape (not true spheres or cubes) as well as the departure of the dielectric function from that in the bulk. However, the experiment validates the tunability of dielectric Mie resonances in submicron CuO particles with size and shape. Further, the experiment validates the large scattering cross sections predicted by FDTD simulations. In particular, the strong Mie resonance at 725 nm in Figure 4e is associated with a giant cross section of $8.8 \times 10^{-13} \ \mathrm{m}^2$.

CONCLUSIONS

Here, we show by experiment and simulation that subwavelength CuO spheres and cubes host dielectric Mie resonances, which are tunable with geometry. Additionally, we have analyzed the characteristics of the lowest energy resonance and the next, which exhibit dipolar- and quadrupolar-like field distributions, respectively. We also reveal these resonances involve both electric and magnetic contributions, where field concentrations occur both inside and on the surface of the particle. The tunability of the Mie resonance peaks in the visible-to-near-IR region can be achieved by controlling the shape and size. Being a strong dielectric resonator, a CuO cube or sphere exhibits strong electric and magnetic field enhancements over the incident light at Mie resonances. Based on these findings, we conclude CuO nanostructures have the promise of being efficient optical antennas for concentrating and manipulating light. Hence, they are good alternatives to PMNs in nanophotonics applications.

ASSOCIATED CONTENT

Supporting Information

The Supporting Information is available free of charge at https://pubs.acs.org/doi/10.1021/acs.jpcc.2c04646.

Detailed descriptions of nanoparticle syntheses and characterization procedures, FDTD simulations, and supporting figures (PDF)

AUTHOR INFORMATION

Corresponding Authors

A. Kaan Kalkan — School of Mechanical and Aerospace Engineering, Oklahoma State University, Stillwater, Oklahoma 74078, United States; oocid.org/0000-0001-5878-3413; Email: kaan.kalkan@okstate.edu

Marimuthu Andiappan — School of Chemical Engineering, Oklahoma State University, Stillwater, Oklahoma 74078, United States; orcid.org/0000-0002-4211-030X; Email: mari.andiappan@okstate.edu

Authors

Sundaram Bhardwaj Ramakrishnan — School of Chemical Engineering, Oklahoma State University, Stillwater, Oklahoma 74078, United States

Nishan Khatri – School of Mechanical and Aerospace Engineering, Oklahoma State University, Stillwater, Oklahoma 74078, United States

Ravi Teja Addanki Tirumala — School of Chemical Engineering, Oklahoma State University, Stillwater, Oklahoma 74078, United States

Farshid Mohammadparast — School of Chemical Engineering, Oklahoma State University, Stillwater, Oklahoma 74078, United States

Krishnageetha Karuppasamy – Department of Computer Science, Oklahoma State University, Stillwater, Oklahoma 74078, United States

Complete contact information is available at: https://pubs.acs.org/10.1021/acs.jpcc.2c04646

Author Contributions

S.B.R., N.K., and R.T.A.T. contributed equally to this work.

The authors declare no competing financial interest.

ACKNOWLEDGMENTS

The authors gratefully acknowledge Dr. M.A.'s awarded funding from the National Science Foundation, CBET Catalysis Program under Grant No. NSF CBET-2102238. The authors also acknowledge funding from the Oklahoma Center for the Advancement of Science and Technology under Project Number HR18-093. Dr. A.K.K. acknowledges National Science Foundation Award # 1707008. Some of the TEM images were acquired at the Oklahoma State University (OSU) Microscopy Laboratory. The authors thank Dr. James Puckette for helping them with using the XRD facility at the Noble Research Center, Oklahoma State University.

REFERENCES

- (1) Bharadwaj, P.; Deutsch, B.; Novotny, L. Optical Antennas. Adv. Opt. Photonics 2009, 1, 438.
- (2) Novotny, L.; van Hulst, N. Antennas for Light. *Nat. Photonics* **2011**, *5*, 83–90.
- (3) Famularo, N. R.; Kang, L.; Li, Z.; Zhao, T.; Knappenberger, K. L.; Keating, C. D.; Werner, D. H. Linear and Nonlinear Chiroptical Response from Individual 3D Printed Plasmonic and Dielectric Micro-Helices. *J. Chem. Phys.* **2020**, *153*, No. 154702.
- (4) Novotny, L.; Stranick, S. J. Near-Field Optical Microscopy and Spectroscopy with Pointed Probes. *Annu. Rev. Phys. Chem.* **2006**, *57*, 303–331.
- (5) Kalkan, A. K.; Fonash, S. J. Laser-Activated Surface-Enhanced Raman Scattering Substrates Capable of Single Molecule Detection. *Appl. Phys. Lett.* **2006**, *89*, No. 233103.
- (6) Singhal, K.; Kalkan, A. K. Surface-Enhanced Raman Scattering Captures Conformational Changes of Single Photoactive Yellow Protein Molecules under Photoexcitation. *J. Am. Chem. Soc.* **2010**, 132, 429–431.
- (7) Jarrett, J. W.; Zhao, T.; Johnson, J. S.; Knappenberger, K. L. Investigating Plasmonic Structure-Dependent Light Amplification and Electronic Dynamics Using Advances in Nonlinear Optical Microscopy. *J. Phys. Chem. C* **2015**, *119*, 15779–15800.
- (8) Tang, L.; Kocabas, S. E.; Latif, S.; Okyay, A. K.; Ly-Gagnon, D.-S.; Saraswat, K. C.; Miller, D. A. B. Nanometre-Scale Germanium Photodetector Enhanced by a near-Infrared Dipole Antenna. *Nat. Photonics* **2008**, *2*, 226–229.

- (9) Cao, L.; Park, J.-S.; Fan, P.; Clemens, B.; Brongersma, M. L. Resonant Germanium Nanoantenna Photodetectors. *Nano Lett.* **2010**, 10, 1229–1233.
- (10) Anker, J. N.; Hall, W. P.; Lyandres, O.; Shah, N. C.; Zhao, J.; Van Duyne, R. P. Biosensing with Plasmonic Nanosensors. *Nat. Mater.* **2008**, 7, 442–453.
- (11) Schuller, J. A.; Taubner, T.; Brongersma, M. L. Optical Antenna Thermal Emitters. *Nat. Photonics* **2009**, *3*, 658–661.
- (12) Nguyen, S. C.; Zhang, Q.; Manthiram, K.; Ye, X.; Lomont, J. P.; Harris, C. B.; Weller, H.; Alivisatos, A. P. Study of Heat Transfer Dynamics from Gold Nanorods to the Environment via Time-Resolved Infrared Spectroscopy. *ACS Nano* **2016**, *10*, 2144–2151.
- (13) Marimuthu, A.; Christopher, P.; Linic, S. Design of Plasmonic Platforms for Selective Molecular Sensing Based on Surface-Enhanced Raman Spectroscopy. *J. Phys. Chem. C* **2012**, *116*, 9824–9829.
- (14) Devaux, E.; Laluet, J.-Y.; Stein, B.; Genet, C.; Ebbesen, T.; Weeber, J.-C.; Dereux, A. Refractive Micro-Optical Elements for Surface Plasmons: From Classical to Gradient Index Optics. *Opt. Express* **2010**, *18*, 20610–20619.
- (15) Christopher, P.; Xin, H.; Andiappan, M.; Linic, S. Singular Characteristics and Unique Chemical Bond Activation Mechanisms of Photocatalytic Reactions on Plasmonic Nanostructures. *Nat. Mater.* **2012**, *11*, 1044–1050.
- (16) Ramakrishnan, S. B.; Tirumala, R. T. A.; Mohammadparast, F.; Mou, T.; Le, T.; Wang, B.; Andiappan, M. Plasmonic Photocatalysis. *Catalysis* **2021**, 38–86.
- (17) DeSario, P. A.; Pietron, J. J.; Dunkelberger, A.; Brintlinger, T. H.; Baturina, O.; Stroud, R. M.; Owrutsky, J. C.; Rolison, D. R. Plasmonic Aerogels as a Three-Dimensional Nanoscale Platform for Solar Fuel Photocatalysis. *Langmuir* **2017**, *33*, 9444–9454.
- (18) DeSario, P. A.; Pietron, J. J.; Brintlinger, T. H.; McEntee, M.; Parker, J. F.; Baturina, O.; Stroud, R. M.; Rolison, D. R. Oxidation-Stable Plasmonic Copper Nanoparticles in Photocatalytic TiO2 Nanoarchitectures. *Nanoscale* **2017**, *9*, 11720–11729.
- (19) Lee, S. A.; Link, S. Chemical Interface Damping of Surface Plasmon Resonances. *Acc. Chem. Res.* **2021**, *54*, 1950–1960.
- (20) Jain, P. K.; Manthiram, K.; Engel, J. H.; White, S. L.; Faucheaux, J. A.; Alivisatos, A. P. Doped Nanocrystals as Plasmonic Probes of Redox Chemistry. *Angew. Chem., Int. Ed.* **2013**, *52*, 13671–13675.
- (21) Li, J.; Cushing, S. K.; Meng, F.; Senty, T. R.; Bristow, A. D.; Wu, N. Plasmon-Induced Resonance Energy Transfer for Solar Energy Conversion. *Nat. Photonics* **2015**, *9*, 601–607.
- (22) Thrithamarassery Gangadharan, D.; Xu, Z.; Liu, Y.; Izquierdo, R.; Ma, D. Recent Advancements in Plasmon-Enhanced Promising Third-Generation Solar Cells. *Nanophotonics* **2017**, *6*, 153–175.
- (23) Jang, Y. H.; Jang, Y. J.; Kim, S.; Quan, L. N.; Chung, K.; Kim, D. H. Plasmonic Solar Cells: From Rational Design to Mechanism Overview. *Chem. Rev.* **2016**, *116*, 14982–15034.
- (24) Feng, L.; Niu, M.; Wen, Z.; Hao, X. Recent Advances of Plasmonic Organic Solar Cells: Photophysical Investigations. *Polymers* **2018**, *10*, No. 123.
- (25) Pala, R. A.; White, J.; Barnard, E.; Liu, J.; Brongersma, M. L. Design of Plasmonic Thin-Film Solar Cells with Broadband Absorption Enhancements. *Adv. Mater.* **2009**, *21*, 3504–3509.
- (26) Cai, Y.-Y.; Tauzin, L. J.; Ostovar, B.; Lee, S.; Link, S. Light Emission from Plasmonic Nanostructures. *J. Chem. Phys.* **2021**, *155*, No. 060901.
- (27) Cushing, S. K.; Bristow, A. D.; Wu, N. Theoretical Maximum Efficiency of Solar Energy Conversion in Plasmonic Metal–Semiconductor Heterojunctions. *Phys. Chem. Chem. Phys.* **2015**, 17, 30013–30022.
- (28) Cushing, S. K.; Li, J.; Bristow, A. D.; Wu, N. In Above and below Band Edge Light Recovery with Plasmonics, Proceedings of Physics, Simulation, and Photonic Engineering of Photovoltaic Devices IV, SPIE OPTO, 2015, San Francisco, California; Freundlich, A.; Guillemoles, J.-F.; Sugiyama, M., Eds.; 2015; p 935811.
- (29) Mohammadparast, F.; Dadgar, A. P.; Tirumala, R. T. A.; Mohammad, S.; Topal, C. O.; Kalkan, A. K.; Andiappan, M. C-C

- Coupling Reactions Catalyzed by Gold Nanoparticles: Evidence for Substrate-Mediated Leaching of Surface Atoms Using Localized Surface Plasmon Resonance Spectroscopy. *J. Phys. Chem. C* **2019**, 123, 11539—11545.
- (30) Mohammadparast, F.; Teja Addanki Tirumala, R.; Bhardwaj Ramakrishnan, S.; Dadgar, A. P.; Andiappan, M. Operando UV–Vis Spectroscopy as Potential in-Line PAT System for Size Determination of Functioning Metal Nanocatalysts. *Chem. Eng. Sci.* **2020**, 225, No. 115821.
- (31) Ramakrishnan, S. B.; Mohammadparast, F.; Dadgar, A. P.; Mou, T.; Le, T.; Wang, B.; Jain, P. K.; Andiappan, M. Photoinduced Electron and Energy Transfer Pathways and Photocatalytic Mechanisms in Hybrid Plasmonic Photocatalysis. *Adv. Opt. Mater.* **2021**, *9*, No. 2101128.
- (32) Addanki Tirumala, R. T.; Ramakrishnan, S. B.; Mohammadparast, F.; Khatri, N.; Arumugam, S. M.; Tan, S.; Kalkan, A. K.; Andiappan, M. Structure—Property—Performance Relationships of Dielectric Cu2O Nanoparticles for Mie Resonance-Enhanced Dye Sensitization. ACS Appl. Nano Mater. 2022, 5, 6699—6707.
- (33) Guo, Z.-Z. Effect of Dielectric Environment on Plasmonic Resonance Absorption of Graphene Nanoribbon Arrays. *Int. J. Mod. Phys. B* **2018**, 32, No. 1850284.
- (34) Maier, S. A.; Atwater, H. A. Plasmonics: Localization and Guiding of Electromagnetic Energy in Metal/Dielectric Structures. *J. Appl. Phys.* **2005**, *98*, No. 011101.
- (35) Kuznetsov, A. I.; Miroshnichenko, A. E.; Brongersma, M. L.; Kivshar, Y. S.; Luk'yanchuk, B. Optically Resonant Dielectric Nanostructures. *Science* **2016**, 354, No. aag2472.
- (36) Kim, S. J.; Thomann, I.; Park, J.; Kang, J.-H.; Vasudev, A. P.; Brongersma, M. L. Light Trapping for Solar Fuel Generation with Mie Resonances. *Nano Lett.* **2014**, *14*, 1446–1452.
- (37) Mohammadparast, F.; Ramakrishnan, S. B.; Khatri, N.; Tirumala, R. T. A.; Tan, S.; Kalkan, A. K.; Andiappan, M. Cuprous Oxide Cubic Particles with Strong and Tunable Mie Resonances for Use as Nanoantennas. ACS Appl. Nano Mater. 2020, 3, 6806–6815.
- (38) Alessandri, I.; Lombardi, J. R. Enhanced Raman Scattering with Dielectrics. *Chem. Rev.* **2016**, *116*, 14921–14981.
- (39) Brongersma, M. L.; Cui, Y.; Fan, S. Light Management for Photovoltaics Using High-Index Nanostructures. *Nat. Mater.* **2014**, 13, 451–460.
- (40) Geffrin, J. M.; García-Cámara, B.; Gómez-Medina, R.; Albella, P.; Froufe-Pérez, L. S.; Eyraud, C.; Litman, A.; Vaillon, R.; González, F.; Nieto-Vesperinas, M.; Sáenz, J. J.; Moreno, F. Magnetic and Electric Coherence in Forward- and Back-Scattered Electromagnetic Waves by a Single Dielectric Subwavelength Sphere. *Nat. Commun.* 2012, 3, No. 1171.
- (41) Sain, B.; Meier, C.; Zentgraf, T. Nonlinear Optics in All-Dielectric Nanoantennas and Metasurfaces: A Review. *Adv. Photonics* **2019**, *1*, 1.
- (42) Tirumala, R. T. A.; Gyawali, S.; Wheeler, A.; Ramakrishnan, S. B.; Sooriyagoda, R.; Mohammadparast, F.; Khatri, N.; Tan, S.; Kalkan, A. K.; Bristow, A. D.; Andiappan, M. Structure—Property—Performance Relationships of Cuprous Oxide Nanostructures for Dielectric Mie Resonance-Enhanced Photocatalysis. *ACS Catal.* **2022**, *12*, 7975—7985.
- (43) Copyright. In *Handbook of Optical Constants of Solids*; Palik, E. D., Ed.; Academic Press: Boston, 1998; p iv.
- (44) Zhang, S.; Jiang, R.; Xie, Y.-M.; Ruan, Q.; Yang, B.; Wang, J.; Lin, H.-Q. Colloidal Moderate-Refractive-Index Cu ₂ O Nanospheres as Visible-Region Nanoantennas with Electromagnetic Resonance and Directional Light-Scattering Properties. *Adv. Mater.* **2015**, *27*, 7432–7439
- (45) Alhassan, W. A. A.; Wadi; Ismael, A. Determination of Optical Energy Gap for Copper Oxide at Different Temperatures. *Int. J. Adv. Eng. Res. Sci.* **2018**, *5*, 255–258.
- (46) Singh, P. K.; Kumar, P.; Hussain, M.; Das, A. K.; Nayak, G. C. Synthesis and Characterization of CuO Nanoparticles Using Strong

Base Electrolyte through Electrochemical Discharge Process. *Bull Mater. Sci.* **2016**, 39, 469–478.

- (47) Clayton, C. K.; Sohn, H. Y.; Whitty, K. J. Oxidation Kinetics of Cu2O in Oxygen Carriers for Chemical Looping with Oxygen Uncoupling. *Ind. Eng. Chem. Res.* **2014**, *53*, 2976–2986.
- (48) Zhu, Y.; Mimura, K.; Isshiki, M. Oxidation Mechanism of Cu2O to CuO at 600-1050 °C. Oxid. Met. 2004, 62, 207–222.
- (49) Dhineshbabu, N. R.; Rajendran, V.; Nithyavathy, N.; Vetumperumal, R. Study of Structural and Optical Properties of Cupric Oxide Nanoparticles. *Appl. Nanosci.* **2016**, *6*, 933–939.
- (50) García-Etxarri, A.; Gómez-Medina, R.; Froufe-Pérez, L. S.; López, C.; Chantada, L.; Scheffold, F.; Aizpurua, J.; Nieto-Vesperinas, M.; Sáenz, J. J. Strong Magnetic Response of Submicron Silicon Particles in the Infrared. *Opt. Express* **2011**, *19*, 4815–4826.
- (51) Poizot, P.; Hung, C.-J.; Nikiforov, M.; Bohannan, E.; Switzer, J. An Electrochemical Method for CuO Thin Film Deposition From Aqueous Solution. *Electrochem. Solid-State Lett.* **2003**, *6*, C21.
- (52) Oh, G.-H.; Hwang, H.-J.; Kim, H.-S. Effect of Copper Oxide Shell Thickness on Flash Light Sintering of Copper Nanoparticle Ink. *RSC Adv.* **2017**, *7*, 17724–17731.
- (53) Kumar, A.; Saxena, A.; De, A.; Shankar, R.; Mozumdar, S. Facile Synthesis of Size-Tunable Copper and Copper Oxide Nanoparticles Using Reverse Microemulsions. *RSC Adv.* **2013**, 3, 5015–5021.
- (54) Azam, A.; Ahmed, A. S.; Oves, M.; Khan, M.; Memic, A. Size-Dependent Antimicrobial Properties of CuO Nanoparticles against Gram-Positive and -Negative Bacterial Strains. *Int. J. Nanomed.* **2012**, 7, 3527–3535.
- (55) Wang, W.; Liu, Z.; Liu, Y.; Xu, C.; Zheng, C.; Wang, G. A Simple Wet-Chemical Synthesis and Characterization of CuO Nanorods. *Appl. Phys. A* **2003**, *76*, 417–420.
- (56) Fang, J.; Xuan, Y. Investigation of Optical Absorption and Photothermal Conversion Characteristics of Binary CuO/ZnO Nanofluids. *RSC Adv.* **2017**, *7*, 56023–56033.
- (57) Diachenko, O.; Kováč, J.; Dobrozhan, O.; Novák, P.; Kováč, J.; Skriniarova, J.; Opanasyuk, A. Structural and Optical Properties of CuO Thin Films Synthesized Using Spray Pyrolysis Method. *Coatings* **2021**, *11*, No. 1392.
- (58) Kreibig, U.; Vollmer, M. Optical Properties of Metal Clusters; Springer: Berlin, 1995; p 31.

☐ Recommended by ACS

Origin of an Anticrossing between a Leaky Photonic Mode and an Epsilon-Near-Zero Point of Silver

Wai Jue Tan, William L. Barnes, et al.

NOVEMBER 03, 2022

THE JOURNAL OF PHYSICAL CHEMISTRY C

READ 🗹

THz Radiation Efficiency Enhancement from Metal-ITO Nonlinear Metasurfaces

Symeon Sideris, Tal Ellenbogen, et al.

DECEMBER 01, 2022

ACS PHOTONICS

READ 🗹

Optical Control over Thermal Distributions in Topologically Trivial and Non-Trivial Plasmon Lattices

Marc R. Bourgeois, David J. Masiello, et al.

OCTOBER 14, 2022 ACS PHOTONICS

READ 🗹

Strong-Field Control of Plasmonic Properties in Core-Shell Nanoparticles

Jeffrey A. Powell, Artem Rudenko, et al.

OCTOBER 28, 2022

ACS PHOTONICS

READ **C**

Get More Suggestions >